Application of a new spectral deconvolution method for in vitro dosimetry in assessment of targeted alpha therapy

Alexis Doudard, Aurélien Corroyer-Dulmont, Cyril Jaudet, Myriam Bernaudin, Samuel Valable, Xavier Ledoux, Anne-marie Frelin-labalme

Application of a new spectral deconvolution method for *in vitro* dosimetry in assessment of targeted alpha therapy

Short title : Spectral analysis for TAT *in vitro* dosimetry

A. Doudard[1], A. Corroyer-Dulmont[2,3], C. Jaudet[2], M. Bernaudin[3], S. Valable[3], X. Ledoux[1], A.M. Frelin-Labalme[1]

[1] *Grand Accélérateur National d'Ions Lourds (GANIL), CEA/DRF CNRS/IN2P3, 14076 Caen, France*

[2] *Medical Physics Department, CLCC François Baclesse, 14000 Caen, France*

[3] *Normandie Univ, UNICAEN, CNRS, ISTCT, GIP CYCERON, 14074 Caen, France*

Abstract

Background: The improvement of *in vitro* assessment of targeted alpha therapy (reproducibility, comparability of experiments…) requires precise evaluation of the dose delivered to the cells. To answer this need, a previous study proposed an innovative dosimetry method based on α-spectroscopy and a specific deconvolution process to recover the spatial distribution of ^{212}Pb isotopes inside *in vitro* culture wells. Nevertheless, although promising, the deconvolution method was time consuming and only tested for a simple isotope decay chain.

Purpose: The purpose of this work is to propose a new matrix deconvolution method of α spectra based on a constrained-non-negative-maximum-likelihood decomposition, both faster and offering a greater modelling flexibility, allowing to study independently the kinetics of each of the daughter nuclides of complex decay chains (illustrated here with ^{223}Ra) in *in vitro* culture wells.

Methods: Firstly, the performance of the new method was fully evaluated through Monte Carlo simulations of *in vitro* irradiations. Different spatial distributions of ^{212}Pb and ^{223}Ra, the corresponding α spectra measured by a silicon detector and the doses delivered to the cells were simulated with Geant4. The deconvolution results were then compared to the simulation results. Secondly, measurements were carried out in culture wells without cells containing 15 kBq of ^{212}Pb or 9.3 kBq of ^{223}Ra, placed above silicon detectors recording α spectra in real time. The matrix deconvolution was then applied to determine the spatial and temporal distribution of all α-emitting daughters of studied isotopes.

Results: The matrix deconvolution was proved to recover the simulated distribution gradients, ensuring simulated doses within 3 % for both tested radionuclides, with errors on dose normally distributed around the reference value (consequently not exhibiting any bias), even in the case of complex decay chains as ^{223}Ra. The experimental study of ^{212}Pb and ^{223}Ra showed highly inhomogeneous distributions and time evolution of the concentration gradients, consistent with the previous study. Furthermore, it highlighted the complex kinetics of ^{223}Ra with different distributions of its α-emitting daughters (^{219}Rn, ^{215}Po, ^{215}At, ^{211}Bi, ^{211}Po).

Conclusions: This study validates a new deconvolution method, fast and flexible, that proved to be accurate and reliable. This method allowed to reveal the complexity of isotopes kinetics in *in vitro* experiments, especially with complex decay chains. Experimental dosimetry, necessary to improve reliability of in vitro studies in targeted alpha therapy, is demonstrated to be feasible with the proposed method.

Keywords: Dosimetry, targeted alpha therapy, *in vitro* irradiation, matrix optimization

Introduction

In the domain of targeted-radionuclide-therapy, Targeted Alpha Therapy (TAT) presents several advantages, particularly for the treatment of small, disseminated metastases and lesions located in sensitive environments.[1] α-particles are characterized by a shorter range in biological tissue covering only a few cell diameters, limiting toxicity to surrounding healthy tissues, but also by their high linear energy transfer (LET) compared to β-particles, which translates into higher cytotoxicity.[2,3] This is supported by developments in radionuclide production and a renewed interest in preclinical and clinical assessments of TAT. [4–6]

During the development of new radiopharmaceuticals, assays are carried out to evaluate their therapeutic interests.[7] *In vitro* assessments occur early in the process, with the main objective of evaluating radiobiological effects, generally as a function of the injected activity inside the culture wells.[8] However, activity is not a relevant metric for assays of α-emitters in many cell configurations, including 2D monolayers where the cells are sensitive to a very small fraction of the injected activity because of the short range of the α-particles. In contrast, the dose delivered to the cells is a more relevant parameter and should be used for TAT assessment[9] through the Medical Internal Radiation Dose (MIRD) formalism.[10] In this formalism, the absorbed dose is proportional to the initial activity injected into the culture well through a global S-factor. However, during the assessment of α-emitters, because of the small range of α-particles in biological matter, this global S-factor is highly dependent on the spatial distribution of the radionuclides inside the culture well. Without knowledge of the spatial distribution, no accurate and reliable dosimetry can be performed. The assumption of a homogeneous distribution of the radionuclides inside the well is most often done with limited consequences when β-emitters of longer ranges are considered, which is no longer the case with α-emitters.[11] Moreover, for a given dose delivered to the cells, the number of hits occurring during in vitro assays is way lower when α-particles are involved with respect to β-particles, the dose deposition from cell to cell thus becoming stochastic.[2,10] Due to geometrical effects, this stochasticity also highly depends on the spatial distribution of emissions.

To address these issues and the lack of adequate dosimetry in this domain, we previously developed an innovative dosimetry method conducted on ^{212}Pb-αVCAM-1 (complexation of ^{212}Pb to an anti-VCAM-1 antibody), for the treatment of early brain metastases.[12,13] In this work, the radioisotopes' spatial and temporal distributions were determined using a silicon semiconductor spectrometer placed below the culture well.[11]

This work confirmed the non-homogeneous distribution of the α-emitters within the well and the importance to use specific methods for this particular purpose. However, this previous deconvolution method required a quite long computing time not compatible with real-time dosimetry and allowed little flexibility on the deconvolution model. Moreover, the previous study was performed with ^{212}Pb which has a relatively simple decay chain, disabling the evaluation of this new dosimetry method for isotopes presenting multiple α-emissions such as ^{225}Ac or ^{223}Ra or forcing the potentially wrong assumption that all the daughter nuclides shared the same time and spatial distribution as the mother nuclide.

This study presents improvements in the spectral deconvolution for the estimation of spatial distributions of various α-emitting radionuclides during *in vitro* assays. In a first part, the new deconvolution method, based on a derivation of the Non-Negative-Least-Squares (NNLS) optimization framework, is evaluated. Precision and accuracy of the method are demonstrated through the deconvolution of simulated spatial distributions representative of *in vitro* experiments. In a second part, this new method is applied to experimental spectra acquired in culture wells to study the kinetic of ^{212}Pb and ^{223}Ra and their α-emitting daughters in *in vitro* conditions.

1. Material & Methods

1.1. *In vitro* assessment in TAT

1.1.1. Experimental setup

Four custom culture wells were built as cylinders of 15 mm diameter carved into a 5 mm-thick PMMA plate. To allow transmission of the α-particles towards the detectors, the base of the wells consisted of a 2.5-µm film of mylar. The measurements were first carried out without cells. Nevertheless, this conception considered that the wells are supposed to receive up to 50 000 cells deposited as a monolayer at their bottom and 2 mm of culture medium, in which a typical activity of 15 kBq of radiopharmaceutical is diluted.[13] Cell culture seeding on the custom culture wells has been assessed through immunochemistry. (see Supplementary Materials).

A passivated ion-implanted silicon semiconductor was placed directly under each well to perform energy spectroscopy. The active detection volume is 100 µm-thick, allowing total collection of the energy of the α-particles. The detectors were covered by a 2.5 µm-thick mylar film to prevent contamination, leading to a total thickness of 5 µm of mylar and 1 mm of air (due to the detector geometry) between the culture medium and the detector surface.[11]

1.1.2. Evaluated isotopes

Measurements done before this work[11] with ^{212}Pb were analyzed with a new constrained Non-Negative-Maximum-Likelihood (C-NNML) deconvolution method (see Section 1.2). They consisted of wells filled with an initial activity of 15 kBq of free ^{212}Pb and spectral acquisitions carried out over 20 hours. ^{212}Pb (10.6 hours half-life) decays toward ^{212}Bi (60.5 min half-life) *via* β^-decay. The energies of α-particles emitted during the decay chain of ^{212}Bi are of 6.1 and 8.8 MeV with respective probabilities of 35.1% and 64.9%.

In addition, measurements were performed with Xofigo ($Cl_2{}^{223}$Ra), using the presented custom-made culture wells and detectors. Two wells containing no cells were filled with 2 mm of water containing 9.3 kBq of ^{223}Ra and spectra were acquired for 140 minutes.

^{223}Ra (11.4 days half-life) decay chain is composed of four α and two β^- disintegrations. The associated energies and branching ratios are summarized in **Figure 1**. The α-emitting isotopes of the ^{223}Ra decay chain can be grouped in four α-emitting groups relative to their decay time and branching ratios. For example, it is reasonable to assume that ^{215}Po and ^{215}At share the same spatial distribution and can be treated as a single radiation source.

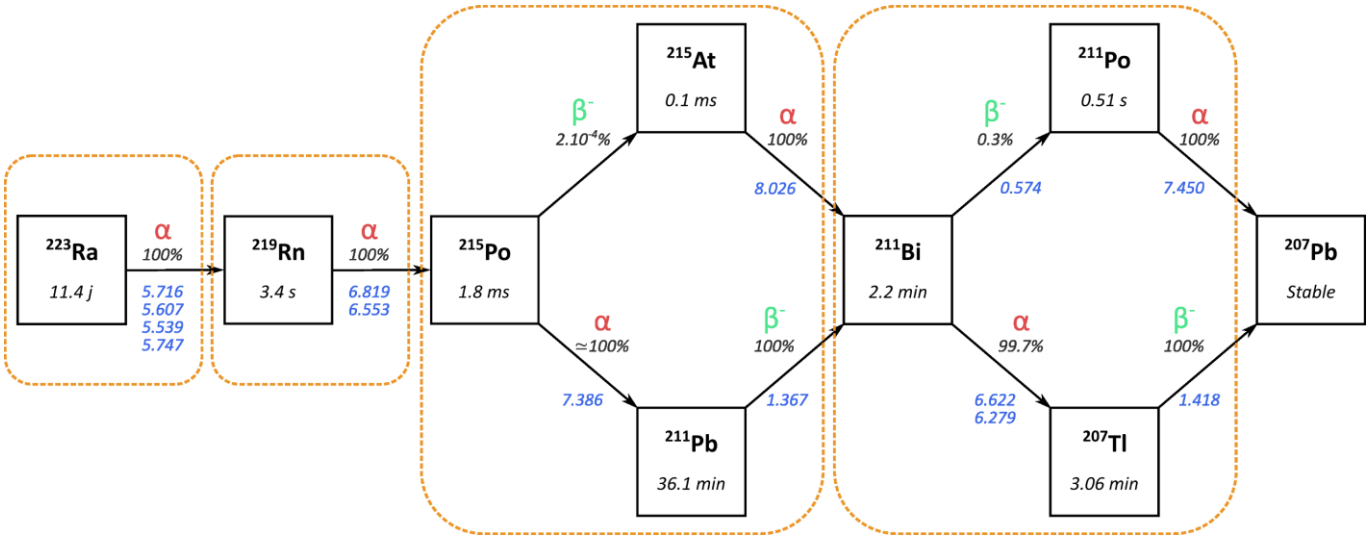

Figure 1 : Decay scheme of ^{223}Ra. Under each radionuclide is indicated its half-life. For α-decays, the main emission energies are indicated under the corresponding arrows (at least 90% of emissions). For β-decays, the principal maximum emission energies are indicated under the corresponding arrows (at least 90% of emissions), except for the ^{215}Po β-decay of unknown energy. The yellow boxes correspond to the different α-decay groups.

1.1.3. Energy spectra acquisition

Energy spectra were acquired with integration times of 5 or 10 minutes, depending on the temporal resolution needed to characterize the kinetics of the isotopes during the irradiation. Spectra bins had a width of 25 keV and were sampled between 1.2 and 9.0 MeV for ^{212}Pb, and between 0.8 and 7.1 MeV for ^{223}Ra. The low energy thresholds eliminate contributions to the energy spectra from γ and X-rays, as well as Auger and internal conversion electrons also emitted in both ^{212}Pb and ^{223}Ra decay chains.

1.1.4. Simulation of *in vitro* experiments

The experimental setups were reproduced under the GEANT4 framework (version 10.6.2).[14,15] To perform dose calculations, the bottom of the well was filled with cells evenly distributed on top of the mylar foil with a sunflower seeding algorithm.[16] Cells were modeled as water half-ellipsoids with 15 µm and 25 µm horizontal half-lengths and a height of 20 µm. A random rotation was applied to each of them. In the case of 212Pb-αVCAM-1 irradiations, there is no specific binding of the radiopharmaceutical to the cells . Consequently, in this study, disintegrations were only simulated from outside of the cells. Energy cuts of 20 µm (characteristic length of a cell) were applied to all particles. Cuts were reduced to 1 µm in the culture medium, from the bottom of the well up to 50 µm height and inside the detector to accurately compute dose deposition and detector signal generation.[17] Simulations were run using the QGSP_BIC_HP_EMZ physics list, particularly adapted to dosimetry in the considered energy range.[15]

The α-emission spectrum of the considered isotope (^{212}Pb or ^{223}Ra) was simulated. All the emissions of the decay chain excluding α-emissions were also simulated separately to compute their dose contribution to the cells. α-emissions were simulated following their branching ratios, while the other particles' emissions were simulated using the GEANT4 RadioactiveDecay module[18] (version 5.4). In the case of ^{223}Ra, since the successive decays of the daughter nuclides occur at significantly different times, thus leading to distinct spatial and temporal distributions, four α-emitting groups (see **Figure 1**) were identified and simulated individually.

1.2. Matrix deconvolution method

The shape of an α-energy spectrum measured by the detectors is more complex than the simple emission spectrum of the radionuclide studied, due to the very short range and high LET of α-particles in water. Consequently, the energy of α-particles reaching the detector do not only depend on their initial energy but also on the thickness of material crossed before reaching the detector. The deconvolution method presented in this study recovers the distribution of crossed thicknesses, and consequently the activity spatial distribution, from measured energy spectra.

This method performs a decomposition of the experimental spectra on a basis of elementary spectra. In this study, it was considered that the spatial distribution of the radionuclides inside the culture wells is only a function of the vertical distance z between the bottom of the well and the location of the disintegration. The culture medium volume was therefore divided into a number n of cylinders characterized by their distance z_i to the bottom of the well and their height h_i, each containing a homogeneous activity. MC simulations were run to compute the average energy spectra produced in the detector by each elementary cylinder. Only α-emissions were simulated, considered the sole contributors to the signal in the detectors. To account for geometric efficiency and energy attenuation, the number of simulated particles was increased progressively from $2.5 \cdot 10^7$ to $2.1 \cdot 10^9$ with the altitude of the cylinder sources, making up for the decrease in probability of signal production. This was done for both ^{212}Pb and ^{223}Ra decay chains. In the case of ^{223}Ra, each α-emitter group of the chain (see **Figure 1**) was simulated individually. The simulation conditions for the basis construction and some elementary spectra for ^{212}Pb are presented in **Figure 2**.

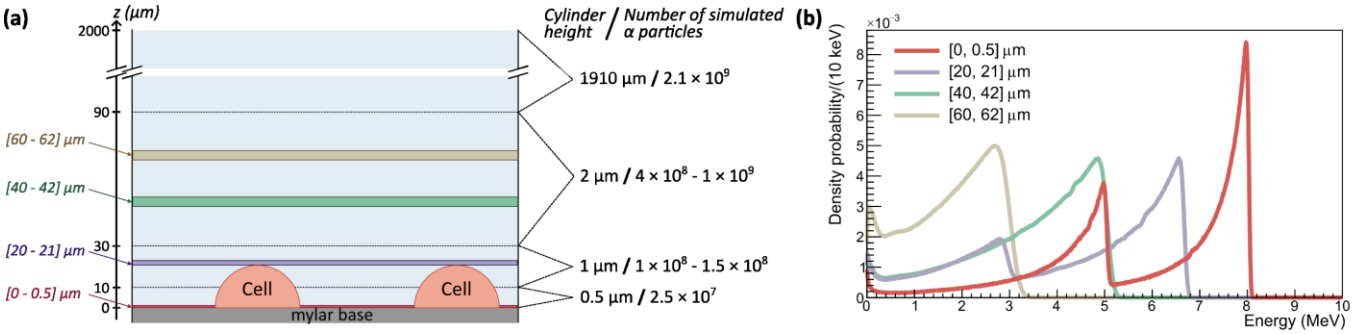

Figure 2: (a) Scheme of the spatial discretization of the culture wells. On the right-hand-side, heights of the cylinders and the number of particles simulated as a function of the height in the well are indicated. (b) Four spectra of the ^{212}Pb deconvolution basis, sampled from the cylinders represented of the same color on the left plot. The legend indicates the minimal and maximal heights of the cylinder from which α-particles were emitted.

Spectra were normalized to the height of their cylinder and their number of simulated primary particles, thus constituting a basis of elementary energy spectra $SP_X(z_i, E)$ for the deconvolution. It was then assumed that any given measured spectrum $SP_Y(E)$ may be decomposed on this basis as :

$$SP_y(E) = \sum_{i=1}^{n} a(z_i) \cdot SP_X(z_i, E) \quad (1)$$

where $a(z_i)$ is proportional to the concentration of radionuclides in the cylinder located at the height z_i. *Equation (1)* can also be expressed as:

$$\boldsymbol{y} = \boldsymbol{Xa} \quad (2)$$

with $\boldsymbol{y}$ the vector corresponding to the experimental spectrum, $\boldsymbol{X} = [SP_X(z_i, E)]$ the matrix containing the simulated spectra basis and $\boldsymbol{a}$ the vector of local activities. The resolution of this equation for $\boldsymbol{a}$ was performed by C-NNML optimization. This optimization process is solved iteratively for a chosen k-th order derivative of the activity distribution vector $\boldsymbol{a^{(k)}} = \boldsymbol{D_k} \cdot \boldsymbol{a}$, written as

$$\boldsymbol{a_{n+1}} = \boldsymbol{D_k^{-1}} \cdot \min_{\boldsymbol{a^{(k)} \geq 0}} \frac{1}{\boldsymbol{\Lambda_n}} \left\| \begin{pmatrix} \boldsymbol{X} \\ p \cdot \boldsymbol{h^T} \end{pmatrix} \cdot \boldsymbol{D_k^{-1}} \boldsymbol{a^{(k)}} - \begin{pmatrix} \boldsymbol{y} \\ p \cdot A_0 \end{pmatrix} \right\|_2^2 \quad (3)$$

The resolution of this equation guaranties an activity gradient toward the bottom of the well (observed in previous study[11]) thanks to the k-th order derivation matrix $\boldsymbol{D_k}$ that enforce monotony of the lower order derivatives of the solution. It also constrains the activity associated to the solution, equal to $\boldsymbol{h^T}.\boldsymbol{a}$ with $\boldsymbol{h}$ the vector of the elementary cylinders' heights, to be equal to the injected activity A_0, using a penalty weight p. $\boldsymbol{\Lambda_n}$ is a weighting matrix enabling likelihood optimization. The definition of *Equation (3)* and its components are detailed in the Supplementary Materials. [19–21] At last, the C-NNML optimization considers the low-counts nature of spectra and reduces overfit phenomena caused by the uneven distribution of the information in the basis of elementary spectra.

Starting from an initial distribution a_0 chosen as homogeneous, the iterative process always converged within five iterations. Consequently, to avoid the election of a poor criterion on convergence, all computations were performed with ten iterations. Uncertainties on a NNLS-problem solution are not algebraically computable.[22] Activity concentration uncertainties were thus estimated by creating a large number of virtual spectra (typically 500) through convolution of the spectrum with a Poisson distribution in each energy bin. All generated spectra were fitted with the same deconvolution process, providing a statistical study of the deconvolution solution. The computational time required to perform one fit depends on the shape of the spectrum and the size of the basis but was systematically below 0.1 s (assessed with a Lenovo laptop under Ubuntu 22.04 LTS, with an Intel Core i7-8750H CPU and 4 GB RAM). The addition of uncertainty computations increases the total computing to less than one minute for any spectrum.

1.3. Evaluation of the deconvolution method

In order to validate and characterize the accuracy of the deconvolution with C-NNML, *in vitro* irradiations were simulated, following the procedure of Section 1.1.4, to build a database of simulated energy spectra in the detector volume and simulated absorbed dose to cells, corresponding to predefined activity concentration

distributions. The evaluation then consisted in comparing the distributions computed by deconvolution of the simulated spectra to the predefined distributions. The impact of potential discrepancies on dose measurement was also evaluated by comparing the simulated absorbed dose to the dose corresponding to the computed distribution.

1.3.1. Predefined spatial distributions

The spatial distributions of activities along the vertical axis were chosen to be plausible in the light of the previous observations.[11] In the case of ^{212}Pb, five different functions were chosen to model distributions presenting a concentration gradient at the bottom of the well: an exponential, a bi-exponential, an inverse power, an exponential with a repulsion term at the bottom, and a constant. All functions were normalized to the total injected activity. Three activities were tested: 14 kBq which is slightly inferior to the initial activity injected during ^{212}Pb assays,[11,13] 10.5 kBq which is representative of activity at the end of the assays, and 3.9 kBq which covers the possibilities for running assays with a lower initial activity or with shorter-lived isotopes. The number of particles simulated was chosen to correspond to 600 s integration times.

The simulation was reproduced 10 times for each distribution function-activity pair, creating a database of 150 spectra with their corresponding doses to the cells for assessment of the methodology with ^{212}Pb.

A similar assessment was done in the case of ^{223}Ra, simulating 60 spectra corresponding to 300 s irradiations with an activity of 9 kBq. To account for the possibility for the different α-emitters of the ^{223}Ra decay chain to have different activity distributions, the four radionuclide groups identified in **Figure 1** were simulated individually. Nevertheless, given the very fast decay of ^{215}Po following the decay of ^{219}Rn, and to prevent overfitting, ^{219}Rn and ^{215}Po were constrained to share the same activity distribution. In the light of the experimental data (see section 2.2.2), three realistic distributions (two bi-exponentials and an inverse power-law) were tested for the three radionuclide groups. In each simulation, one of the three distributions was attributed to each isotopes group. Each radionuclide distribution amplitude was scaled to reproduce the spectra and gradients observed experimentally. Six different distributions were thus simulated 10 times, generating a database of 60 spectra with their corresponding absorbed doses to the cells.

1.3.2. Absorbed dose to cells

This work focuses on the determination of the spatial distribution of radioisotopes during *in vitro* experiments to accurately determine the absorbed dose to cells. It was thus relevant to assess the impact of the deconvolution with C-NNML on dose computation. To that intent, the dose delivered to the cells and the corresponding uncertainty were calculated from the computed spatial distributions following the MIRD

formalism as the product of the local cumulative activities given by the deconvolution as a function of the distance from the bottom z_i and the corresponding S-factors averaged over the cylinders[10]:

$$D(t) = \sum_i A(t, z_i) \cdot S(z_i) \quad (4)$$

Using the simulation geometry and the spatial sampling given in Section 1.2, the S-factors for α and non-α emissions were determined by MC simulations as a function of the height in the well by simulating a large number of emissions (similar to the description in **Figure 2**). Uncertainties on S-factors were computed to consider the stochastic nature of dose deposition, corresponding to standard deviations on the dose delivered per disintegration. The uncertainty on the mean value of the S-factors was also considered in the uncertainty calculations but was always at least two orders of magnitude lower due to the large number of simulated disintegrations.

2. Results

2.1. Evaluation of the matrix deconvolution method

As described in Section 1.3.1, 210 spectra (150 + 60) and absorbed doses to the cells were simulated, with five different predefined spatial distributions and three different initial activities for ^{212}Pb, and six different spatial distributions with one initial activity and three emitter groups for ^{223}Ra. Simulated spectra were fitted with the C-NNML deconvolution method. Uncertainties were computed including the stochastic uncertainty on the average dose per emission and the uncertainty on the spatial deconvolution solution. This enabled comparisons between deconvoluted and simulated activity distributions as well as simulated doses against their computed counterparts obtained through deconvolution.

2.1.1. Validation for ^{212}Pb irradiations

2.1.1.1. Spatial activity distributions

As shown in **Figure 3** for an injected activity of 14 kBq, based on visual inspection, the simulated spectra are well fitted for all simulated distributions. Even if they are not represented, results are similar for the lower activities.

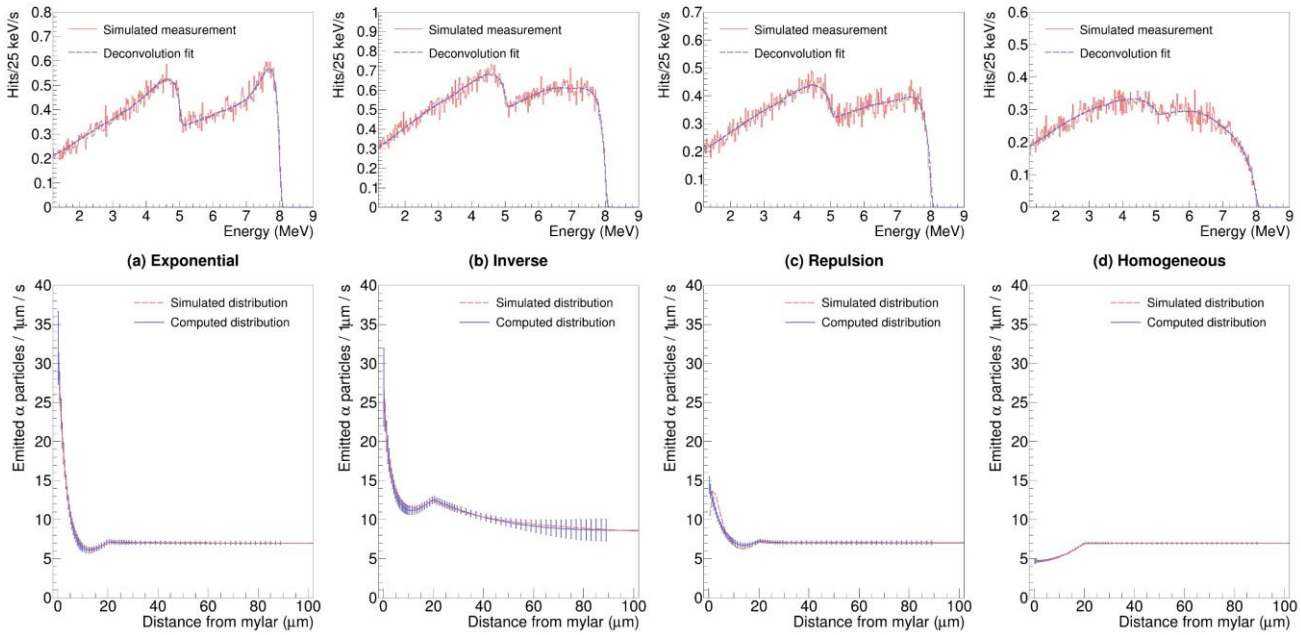

Figure 3: Deconvolution of the spectra simulated with exponential (a), inverse (b), exponential with repulsion (c), and constant (d) spatial distributions of the radionuclides. For each figure, the top plot represents the simulated spectrum (in red, dotted) and the spectral fit (in purple). The bottom plot represents the deconvoluted lineic distribution (in purple) against the simulated distribution (in red, dotted). It must be noted that the lineic distributions differ from the model functions because of the non-internalization of the radionuclides in the cells.

The deconvoluted activity distributions, shown in the bottom row of **Figure 3**, follow the trends of the simulated distributions. As expected, in the case of the repulsion distribution, the deconvolution cannot reproduce the simulated distribution, because it does not respect the proposed model of a concentration gradient toward the bottom of the well. However, a compensation phenomenon is observed with an overestimation and then an underestimation of the distribution below 20 µm. Above this height, the agreement is good. In the case of the inverse function, larger uncertainty bars are observed for the coefficients corresponding to the largest distances from mylar. This is due to the last coefficients being computed as average spatial distributions over larger bins while the actual inverse distribution is still significantly decreasing, unlike the four other distributions based on exponential functions which rapidly decrease to a constant value, and that are thus not sensitive to the averaging process.

2.1.1.2. Delivered dose to the cells

The dose delivered to the cells was deduced from the spatial distribution by application of the cross-product of *Equation 4*. For the 150 dose computations, the relative error (*i.e.,* the relative difference between computed and simulated doses) is always below 3 %. Moreover, the computed uncertainty is reliable, with the

difference between computed and simulated dose being within one standard deviation (s.d.) in 104 cases (69.3 %), within two s.d. in 141 cases (94.0 %), and within three s.d. in 149 cases (99.3 %). Lastly, no bias in the dose computation was identified for any of the distributions (-0.01 % ± 0.19 %), suggesting that the error is normally distributed around the true value. Even with the repulsion distribution, in the 14 kBq total activity case, the average computed dose to the cells is of 19.06 ± 0.06 mGy with an average estimated uncertainty of 0.32 ± 0.01 mGy (three s.d.), compatible with the average ground truth dose of 18.99 ± 0.11 mGy. It can be noted that these results are not compatible with the other tested distributions (see the Supplementary Materials). Separating the α and non-α contributions to the dose, no significant bias appears for the α part (0.08 % ± 0.26 %) while a small bias has been identified for the non-α part (-1.29 % ± 0.07 %). This bias can be explained by the size of 1910 µm of the last spatial bin. The computation of an averaged spatial distribution in this bin, multiplied by an averaged value of a S-factor for non-α emissions that still evolves significantly above the range of detection of the α-particles, leads to an underestimation of this dose contribution.

2.1.2. Validation for ^{223}Ra irradiations

2.1.2.1. Spatial activity distributions

As described in Section 1.3.1, 60 irradiations with ^{223}Ra were simulated, corresponding to ten repetitions of each combination of the different spatial distributions of the three isotope groups. **Figure 4** shows an example of a spectrum fit by the deconvolution process.

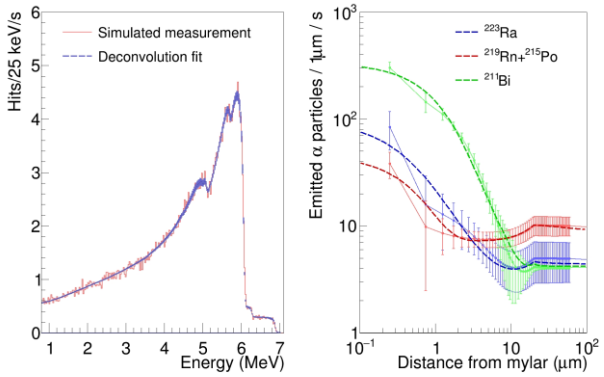

Figure 4 : Spectral deconvolution of a simulated irradiation with ^{223}Ra. The left plot represents a simulated spectrum (in red) and the spectral fit (in blue). The right plot represents the simulated lineic distributions (dotted lines) and the recovered distributions (full lines). Uncertainty bars are given as three s.d.

^{223}Ra spectra analysis showed larger deviations between the deconvoluted and simulated distributions as well as larger associated uncertainties. However, all spectra appeared appropriately fitted, highlighting that the activity distributions are subject to overfitting in the case of multiple α-emitters. The larger size of the base of elementary spectra (actually one per isotope group) and consequently the large number of degrees of freedom is an explanatory factor for the observed overfitting. Nevertheless, as shown by the results on dose computation in the following section, compensation phenomena can take place between the different emitter groups, since it ultimately leads to accurate dose computations.

C-NNML deconvolution is thus effective even with more complex decay chains such as the one of ^{223}Ra to retrieve the gradients for the different spatial distributions, although the coefficients are associated with larger uncertainties and may deviate from the actual distribution.

2.1.2.2. Delivered dose to the cells

For the six different combinations of activity distributions of the three isotope groups, the relative error on dose is always below 2%. However, the simulated dose value is systematically within two s.d. of the computed dose, which could be interpreted as an overestimation of the uncertainty. Further analysis of the results indicated that the α and non-α contributions to the dose were biased, with a systematic slight overestimation of the dose due to α-emissions (0.56 % ± 0.26 %) and underestimation of the dose due to other emissions (-1.72 ± 0.26%). The underestimation of the non-α contribution is of the same nature as that of the one for ^{212}Pb. The bias on the α contribution seems to be due to the overfitting of spatial activities. Individual isotope group doses were indeed associated with large errors in dose for a given spectrum (from -45.4 % to + 27.7 %) ultimately compensating each other.

2.2. Study of ^{212}Pb and ^{223}Ra kinetics in *in vitro* conditions

After the evaluation and validation, the C-NNML deconvolution was applied to experimental spectra acquired in *in vitro* conditions. In a first step, it was tested with ^{212}Pb irradiations performed in our previous work[11] to compare the results of both deconvolution methods and improve the spatial resolution of the activity distribution close to the bottom. In a second step, the spatial distribution of radionuclides was studied for ^{223}Ra irradiations.

2.2.1. Measurements with ^{212}Pb

C-NNML deconvolution was applied to experimental spectra acquired at different times during ^{212}Pb irradiations: t = 0, 15, 65, and 245 min after deposition of the radionuclides inside the well. The spatial activity distributions of ^{212}Pb computed from these spectra with C-NNML and the previous parametric method are presented in **Figure 5**.

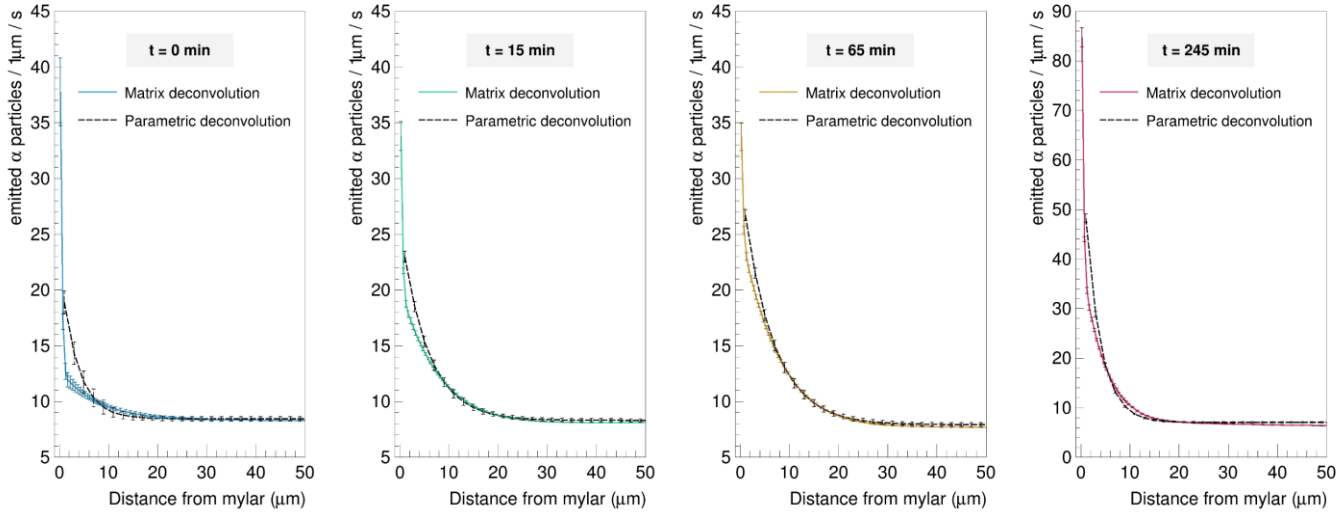

Figure 5: Comparison of spatial activity distribution deconvolutions with C-NNML and the previous parametric method. The deconvoluted spectra were obtained at, from left to right, 0, 15, 65, and 245 min after ^{212}Pb deposition. Uncertainty bars are given as one s.d.

Discrepancies with the parametric method are noticeable. Amplitudes of the gradients computed for the different spectra differ largely, which is explained by the different spatial binning used for the two methods. In the first 10 µm, the matrix method uses 0.5 µm-high bins while the parametric method used only 2 µm-high bins, thus averaging exponential gradients over a larger range, consequently leading to smaller apparent amplitudes. Another difference that seems to occur at the very first measurement times is the presence of a different gradient shape recovered by C-NNML optimization, with a strong discontinuity of the distribution appearing below one µm that is not compatible with the parametric model, exclusively modeling exponential distributions. Finally, for all spectra, the last bins converged systematically towards slightly larger homogenous concentrations for the parametric method than for C-NNML. The addition of a constraint on the total activity for the C-NNML method (see Supplementary Materials) makes the constant estimation more reliable, which is useful for β-dose estimation.

This analysis confirmed the complex kinetics governed by a strong concentration gradient at the bottom of the well, and a significant time evolution not caused by the radioactive decay during the 200 first minutes of irradiation. Nevertheless, the new method presented in this study provides a better spatial resolution of the activity distribution close to the bottom of the well, which contributes most to the dose deposition in the cells.

2.2.2. Measurements with ^{223}Ra

C-NNML deconvolution was also applied to energy spectra acquired for a well containing 9.3 kBq of ^{223}Ra in the experimental conditions described in Section 1.1. Spectra were acquired during 140 min with five min integration times.

As shown in **Figure 6a** for two acquisition times (t = 5 and 25 min), the shape of the spectra significantly varies with time. In particular, the ^{211}Bi peak presents significant variations in amplitude relative to the other isotopes peaks. This means that the radionuclides of the ^{223}Ra decay chain present different kinetics and that the experimental spectra cannot be fitted with a spatial distribution common to all isotopes. The best compromise between the reproduction of experimental spectra and overfitting was determined in terms of Bayesian information criteria. It was obtained by separating three activity distributions for ^{223}Ra, ^{219}Rn plus ^{215}Po, and ^{211}Bi groups. As shown in **Figure 6a**, this separation leads to a good fit of the acquired spectra.

Figures 6b and 6c feature strong concentration gradients for all radionuclides, although the concentration gradients amplitudes and shapes are different between the different groups. In particular, the concentration of ^{211}Bi towards the bottom of the well is much higher than those of the other nuclides from the start of the irradiation. Moreover, as shown in **Figure 6d**, the concentration of ^{211}Bi at the bottom of the wells is more important and subject to a significantly larger evolution during irradiation than the other nuclide groups.

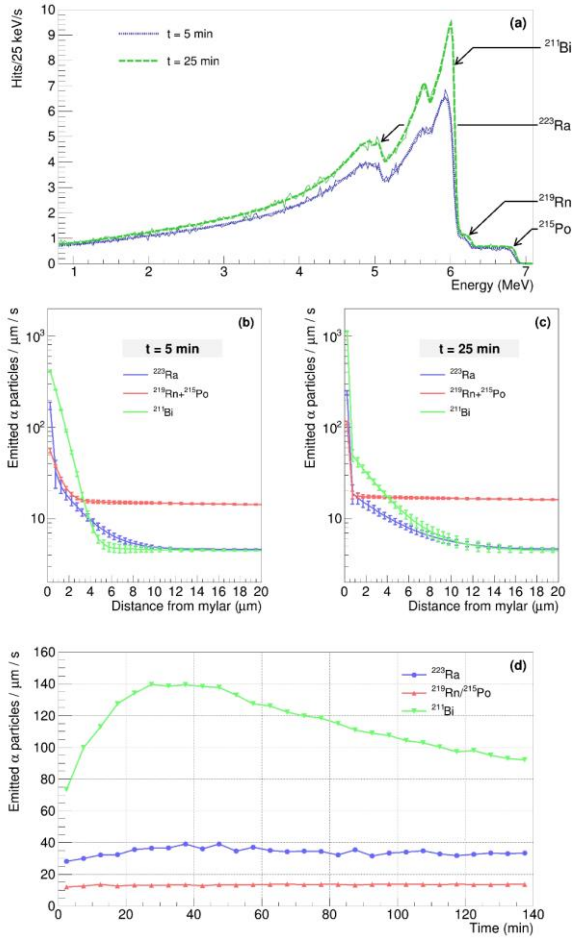

320 *Figure 6 : (a) In full line, energy spectra measured by the detectors 5 min and 25 min after ^{223}Ra deposition in a well, and in dashed lines, fits obtained from C-NNML deconvolution. (b,c) Spatial distributions computed in the first 20 µm at the bottom of the well. Uncertainty bars are given as three s.d. (d) Average activity in the first five µm as a function of time, for the three considered radionuclide groups.*

325 3. Discussion

As previously shown, the early-stage evaluations of α-emitters such as *in vitro* assessments raise new methodology needs. In particular, the widespread use of the injected activity to quantify biological effects is not relevant with α-particles and is expected to cause significant errors.[8] To answer this issue, the determination of the delivered dose to the cells is the most straightforward solution. It nevertheless strongly
330 depends on the spatial distribution of the radionuclides in the culture well and a spatial deconvolution method was previously proposed but required upgrading, validation, and evaluation. In this study, a new method meeting these expectations was developed and assessed.

3.1. Performances of the matrix deconvolution method

The performances of the C-NNML deconvolution were evaluated with ^{212}Pb and ^{223}Ra, which are very different radionuclides. ^{212}Pb has only one α-decay along the chain with two very distinct energies (6.1 and 8.8 MeV). As such, it represents the simplest emission case for proof-checking of the proposed methodology. Assays with ^{223}Ra were also very enlightening because of the more complex decay chain, presenting different α-emissions of closer energies (between 5.5 and 7.4 MeV), thus increasing the overlapping of information. In addition to their proximity, the lower α-particles energies shorten the spatial range that can be accurately probed (about 60 µm instead of 90 µm with ^{212}Pb).

This study (in particular the comparison between the parametric and C-NNML methods) has shown that an insufficient spatial resolution for the deconvolution can lead to errors in the activity estimation at the bottom 10 µm of the well, where the concentration gradient is the largest. This phenomenon was countered by proposing an adaptative decomposition with bins of smaller heights close to the bottom of the well (down to 0.5 µm instead of 2 µm in the previous study). The reduction of the height of the spatial sampling is however limited by the overfit risks associated with increasing the size of the deconvolution basis.

As shown in the case of ^{212}Pb, the matrix deconvolution is very efficient to determine a spatial distribution presenting a concentration gradient towards the bottom of the well. Still, it may be unable to recover distributions not following the constrained model, despite an apparent correct fit of the energy spectrum. It is specifically shown by the distribution presenting a repulsion contribution close to the bottom (see **Figure 3c**). Despite this limit, the computed distribution leads to a delivered dose in agreement with the reference simulated dose (with a reference dose almost systematically included in the computed error bars, and a difference always lower than 3%). It is reasonable to expect similar results in the case of activity distributions globally increasing toward the bottom, but the confirmation would require other experiments, and maybe other experimental conditions.

The method also proved efficient with ^{223}Ra to deconvolve energy spectra generated by more complex decay chains. The individualization of the spatial and temporal distribution of the different radionuclides of the decay chain increases the number of degrees of freedom of the deconvolution, leading to larger biases in the spatial activity computation. Still, these biases compensate for each other, allowing computation of doses in agreement with simulated doses (due to the similarity of the LET of all α-emitters during the traversal of a cell,

the global distribution of all α-emitters is more critical than the individual distributions of each radioisotope), which is ultimately the main purpose of this work.

For both radionuclides, the deconvolution validation highlighted that other biases, albeit limited, may take place at longer distances from the bottom, because the different radionuclides' energy spectra present a strong overlap of information at the lowest energies below the peaks (typically below 4 MeV), causing overfitting in this range. Even if this spatial range has a low impact on the dose delivered by α-particles, it is responsible for a non-negligible part of the dose delivered by β-emissions. This overfitting on the lowest energies was reduced by taking into account the initial activity injected into the well to constrain the deconvolution process (see Supplementary Materials). A consequence of this numerical constraint is that the uncertainty on the injected activity will cause uncertainty on the activity distribution far from the bottom, and consequently, on the dose deposited by β-particles. However, this uncertainty would also be present for an irradiation characterization based on the activity. Moreover, because of the limited contribution of β-particles to the dose deposition, this phenomenon is expected to have limited influence on the total delivered dose uncertainty. The deconvolution of the spatial distribution at longer distances from the bottom could be further improved thanks to the measurement of β-particles in addition to α-particles. This would provide enhanced information on the spatial distribution of radionuclides between 50 µm and the top of the well. This nevertheless would require the implementation of a second detector, dedicated to the detection of β-particles.

It must also be noted that this new C-NNML deconvolution was fully characterized in this work for two α-emitters. A similar validation and evaluation process should be performed for any new radionuclide of interest, to detect potential biases due to the decay chain complexity or emission energies and characterize their intensity. Nonetheless, this process may easily be implemented as it relies on simulated distributions and spectra.

The C-NNML deconvolution also significantly improves the computational speed and the spatial resolution. It can be used in two modes: a “complete” mode that computes the uncertainties on the radionuclides’ concentrations, and a “fast” mode ignoring them. In the complete mode, with the generation of 500 additional spectra for uncertainties estimation of the activity coefficients, a spectrum analysis with uncertainties calculation takes less than a minute when the complete ^{223}Ra basis is used. In the fast mode, this duration decreases to less than one 0.1 s, allowing online measurements, while the previous parametric method was systematically taking more than a minute with the same hardware for a spectral analysis in the simpler case

of ^{212}Pb. Although the fast mode does not consider the spatial distribution uncertainties, the dose value reported by both modes were always comparable, meaning that this mode enables reliable online dosimetry of *in vitro* experiments which should be completed offline by a run of the complete mode to assess the associated uncertainty.

3.2. Study of ^{212}Pb and ^{223}Ra kinetics in *in vitro* conditions

Once evaluated, C-NNML deconvolution was applied to experimental spectra obtained with ^{212}Pb and ^{223}Ra. The analysis of the ^{212}Pb spectra was in agreement with the previous study but provided additional insights into possible uncertainties on the spatial distribution with the previously used exponential model. The two deconvolution methods provided comparable dose computations and the same quality of spectral fits whereas visible discrepancies appeared for the activity distributions, suggesting that the main criterion for reliability of the computed dose is the quality of the spectra fits.

The analysis of the experimental spectra of ^{223}Ra confirmed the complexity of the spatial and temporal activity distributions already observed with ^{212}Pb. Concentration gradients at the bottom of the well and migration of the radionuclides (mainly toward the bottom of the well) during the experiment were observed. Another level of complexity is reached with the differentiation of the different isotopes' spatial and temporal distributions due to their different properties. In particular, ^{211}Bi has a 36 min half-life period and consequently a longer migration time before its α-decay toward ^{207}Tl. ^{219}Rn, the first daughter nuclide of ^{223}Ra, has a quite short half-life period (3.4 s) not in favor of an important migration after the decay of ^{223}Ra, but still exhibits different spatial and temporal distributions that could be attributed to its chemical properties as an ideal gas. All these observations confirm and highlight the complexity of the activity distribution of α-emitters during *in vitro* experiments. Even though these measurements were performed without cells, this reinforces the irrelevance of the injected activity as a quantitative indicator for *in vitro* experiments involving α-emitters and the importance of measuring their spatial and time distributions during the experiment. Of course, the presence of cells and their configuration is expected to modify the spatial distribution as well as the kinetics, especially in the presence of specific targeting molecules. Nevertheless, the complexity will remain and justifies the proposed dosimetry methodology, which will be carried out in future experiments.

3.3. Other sources of uncertainty in *in vitro* dosimetry of α-emitters

The main additional source of uncertainty in *in vitro* dosimetry concerns the determination of the S-factors and consequently the modeling of the dose deposition in cells once the activity distribution is accurately known. Since the main purpose of this study is the determination of the spatial distribution, evenly distributed cells with identical half-ellipsoid shapes were modeled. Even with this schematic geometry, modification of the cell density or dimensions had a direct consequence on the average dose delivered to the cells per disintegration. This is primarily caused by a modification of the distribution of path lengths of α-particles through the cells and the geometric interface between the cells and the activity distribution. To answer the requirement for a more precise modeling of the cell medium, cell imaging will be used in future experiments. This will allow the implementation of cell models adapted to different endpoints (like cell survival or double-strand break rate). Coupling our approach with an appropriate cell modelling and with the more precise Geant4-DNA physics would also enable microdosimetry of *in vitro* assays, particularly relevant in the context of TAT where the number of cell hits are sufficiently low to lead to stochasticity of the dose deposition from cell to cell[7,23]. Finally, this study was performed in the frame of 2D cell cultures. Other biological models could be considered, such as 3D cell spheroids which are more realistically reproducing a tumorous environment[24].

Conclusions

This paper demonstrates the reliability of the novel C-NNML deconvolution for dosimetry during *in vitro* assessments of TAT. The use of simulated *in vitro* irradiations, in perfectly controlled conditions, highlighted that the dose computations following the proposed method are reliably distributed within 3% of the true dose. It also showed that the algorithm may recover with good precision the dose delivered to the cells for true distributions not following the continuous gradient of activity distribution model. Furthermore, experiments with ^{223}Ra proved that the methodology can apply to other α-emitting radiopharmaceuticals with good reliability, even with more complex decay chains. Nonetheless, transposition of the methodology to another radiopharmaceutical should be done carefully, to identify potential sources of biases due to the lifetimes and energies involved in the decay chain.

Acknowledgments

This project has received financial support from the Centre National de la Recherche Scientifique (CNRS) through the MITI interdisciplinary program ISOTOP2020.

Conflicts of interest

The authors declare no conflict of interest.

References

1. Guerard F, Barbet J, Chatal J, Kraeber-Bodere F, Cherel M, Haddad F. Which radionuclide, carrier molecule and clinical indication for alpha-immunotherapy? *Q J Nucl Med Mol Imaging Off Publ Ital Assoc Nucl Med AIMN Int Assoc Radiopharmacol IAR Sect Soc Of*. 2015;59(2):161-167.

2. Pouget JP, Constanzo J. Revisiting the Radiobiology of Targeted Alpha Therapy. *Front Med*. 2021;8:692436. doi:10.3389/fmed.2021.692436

3. Dahle J, Abbas N, S. Bruland O, H. Larsen R. Toxicity and Relative Biological Effectiveness of Alpha Emitting Radioimmunoconjugates. *Curr Radiopharm*. 2011;4(4):321-328.

4. Radchenko V, Morgenstern A, Jalilian AR, et al. Production and Supply of α-Particle–Emitting Radionuclides for Targeted α-Therapy. *J Nucl Med*. 2021;62(11):1495-1503. doi:10.2967/jnumed.120.261016

5. Makvandi M, Dupis E, Engle JW, et al. Alpha-Emitters and Targeted Alpha Therapy in Oncology: from Basic Science to Clinical Investigations. *Target Oncol*. 2018;13(2):189-203. doi:10.1007/s11523-018-0550-9

6. Bruchertseifer F, Kellerbauer A, Malmbeck R, Morgenstern A. Targeted alpha therapy with bismuth-213 and actinium-225: Meeting future demand. *J Label Compd Radiopharm*. 2019;62(11):794-802. doi:10.1002/jlcr.3792

7. Bolch WE, Eckerman KF, Sgouros G, Thomas SR. MIRD Pamphlet No. 21: A Generalized Schema for Radiopharmaceutical Dosimetry—Standardization of Nomenclature. *J Nucl Med*. 2009;50(3):477-484. doi:10.2967/jnumed.108.056036

8. Corroyer-Dulmont A, Jaudet C, Frelin AM, et al. Radioimmunotherapy for Brain Metastases: The Potential for Inflammation as a Target of Choice. *Front Oncol*. 2021;11:714514. doi:10.3389/fonc.2021.714514

9. Humm JL. Dosimetric aspects of radiolabeled antibodies for tumor therapy. *J Nucl Med Off Publ Soc Nucl Med*. 1986;27(9):1490-1497.

10. Sgouros G, Roeske JC, McDevitt MR, et al. MIRD Pamphlet No. 22 (Abridged): Radiobiology and Dosimetry of α-Particle Emitters for Targeted Radionuclide Therapy. *J Nucl Med*. 2010;51(2):311-328. doi:10.2967/jnumed.108.058651

11. Frelin-Labalme A, Roger T, Falzone N, et al. Radionuclide spatial distribution and dose deposition for *in vitro* assessments of ^{212} Pb-αVCAM-1 targeted alpha therapy. *Med Phys*. 2020;47(3):1317-1326. doi:10.1002/mp.13969

12. Falzone N, Ackerman NL, Rosales L de la F, et al. Dosimetric evaluation of radionuclides for VCAM-1-targeted radionuclide therapy of early brain metastases. *Theranostics*. 2018;8(1):292-303. doi:10.7150/thno.22217

13. Corroyer-Dulmont A, Valable S, Falzone N, et al. VCAM-1 targeted alpha-particle therapy for early brain metastases. *Neuro-Oncol*. 2020;22(3):357-368. doi:10.1093/neuonc/noz169

14. Agostinelli S, Allison J, Amako K, et al. Geant4—a simulation toolkit. *Nucl Instrum Methods Phys Res Sect Accel Spectrometers Detect Assoc Equip*. 2003;506(3):250-303. doi:10.1016/S0168-9002(03)01368-8

15. Allison J, Amako K, Apostolakis J, et al. Recent developments in Geant4. *Nucl Instrum Methods Phys Res Sect Accel Spectrometers Detect Assoc Equip*. 2016;835:186-225. doi:10.1016/j.nima.2016.06.125

16. Vogel H. A better way to construct the sunflower head. *Math Biosci*. 1979;44(3-4):179-189. doi:10.1016/0025-5564(79)90080-4

17. Khan AU, DeWerd LA. Evaluation of the GEANT4 transport algorithm and radioactive decay data for alpha particle dosimetry. *Appl Radiat Isot*. 2021;176:109849. doi:10.1016/j.apradiso.2021.109849

18. Hauf S, Kuster M, Batic M, et al. Radioactive Decays in Geant4. *IEEE Trans Nucl Sci*. 2013;60(4):2966-2983. doi:10.1109/TNS.2013.2270894

19. Lawson CL, Hanson RJ. *Solving Least Squares Problems*. Society for Industrial and Applied Mathematics; 1995. doi:10.1137/1.9781611971217

20. Bro R, De Jong S. A fast non-negativity-constrained least squares algorithm. *J Chemom*. 1997;11(5):393-401. doi:10.1002/(SICI)1099-128X(199709/10)11:5<393::AID-CEM483>3.0.CO;2-L

21. McCullagh P, Nelder JA. *Generalized Linear Models*. Springer US; 1989. doi:10.1007/978-1-4899-3242-6

22. Slawski M, Hein M. Non-negative least squares for high-dimensional linear models: Consistency and sparse recovery without regularization. *Electron J Stat*. 2013;7(none). doi:10.1214/13-EJS868

23. Ivanchenko VN, Incerti S, Francis Z, et al. Combination of electromagnetic physics processes for microdosimetry in liquid water with the Geant4 Monte Carlo simulation toolkit. *Nucl Instrum Methods Phys Res Sect B Beam Interact Mater At*. 2012;273:95-97. doi:10.1016/j.nimb.2011.07.048

24. Kapałczyńska M, Kolenda T, Przybyła W, et al. 2D and 3D cell cultures – a comparison of different types of cancer cell cultures. *Arch Med Sci*. Published online 2016. doi:10.5114/aoms.2016.63743

Captions

Figure 1 : Decay scheme of ^{223}Ra. Under each radionuclide is indicated its half-life. For α-decays, the main emission energies are indicated under the corresponding arrows (at least 90% of emissions). For β-decays, the principal maximum emission energies are indicated under the corresponding arrows (at least 90% of emissions), except for the ^{215}Po β-decay of unknown energy. The yellow boxes correspond to the different α-decay groups.

Figure 2: (a) Scheme of the spatial discretization of the culture wells. On the right-hand-side, heights of the cylinders and the number of particles simulated as a function of the height in the well are indicated. (b) Four spectra of the ^{212}Pb deconvolution basis, sampled from the cylinders represented of the same color on the left plot. The legend indicates the minimal and maximal heights of the cylinder from which α-particles were emitted.

Figure 3: Deconvolution of the spectra simulated with exponential (a), inverse (b), exponential with repulsion (c), and constant (d) spatial distributions of the radionuclides. For each figure, the top plot represents the simulated spectrum (in red, dotted) and the spectral fit (in purple). The bottom plot represents the deconvoluted lineic distribution (in purple) against the simulated distribution (in red, dotted). It must be noted that the lineic distributions differ from the model functions because of the non-internalization of the radionuclides in the cells.

Figure 4 : Spectral deconvolution of a simulated irradiation with ^{223}Ra. The left plot represents a simulated spectrum (in red) and the spectral fit (in blue). The right plot represents the simulated lineic distributions (dotted lines) and the recovered distributions (full lines). Uncertainty bars are given as three s.d.

Figure 5: Comparison of spatial activity distribution deconvolutions with C-NNML and the previous parametric method. The deconvoluted spectra were obtained at, from left to right, 0, 15, 65, and 245 min after ^{212}Pb deposition. Uncertainty bars are given as one s.d.

Figure 6 : (a) In full line, energy spectra measured by the detectors 5 min and 25 min after ^{223}Ra deposition in a well, and in dashed lines, fits obtained from C-NNML deconvolution. (b,c) Spatial distributions computed in the first 20 µm at the bottom of the well. Uncertainty bars are given as three s.d. (d) Average activity in the first five µm as a function of time, for the three considered radionuclide groups.